nature structural & molecular biology

ARTICLES

https://doi.org/10.1038/s41594-018-0046-4

Global delay in nascent strand DNA methylation

Jocelyn Charlton[1,2,7], Timothy L. Downing[2,3,6,7], Zachary D. Smith[2,3], Hongcang Gu[3], Kendell Clement[2,3], Ramona Pop[2], Veronika Akopian[2], Sven Klages[1], David P. Santos[4], Alexander M. Tsankov[2,3], Bernd Timmermann[1], Michael J. Ziller[5], Evangelos Kiskinis[4], Andreas Gnirke[3] and Alexander Meissner[1,2,3*]

Cytosine methylation is widespread among organisms and essential for mammalian development. In line with early postulations of an epigenetic role in gene regulation, symmetric CpG methylation can be mitotically propagated over many generations with extraordinarily high fidelity. Here, we combine BrdU labeling and immunoprecipitation with genome-wide bisulfite sequencing to explore the inheritance of cytosine methylation onto newly replicated DNA in human cells. Globally, we observe a pronounced lag between the copying of genetic and epigenetic information in embryonic stem cells that is reconsolidated within hours to accomplish faithful mitotic transmission. Populations of arrested cells show a global reduction of lag-induced intermediate CpG methylation when compared to proliferating cells, whereas sites of transcription factor engagement appear cell-cycle invariant. Alternatively, the cancer cell line HCT116 preserves global epigenetic heterogeneity independently of cell-cycle arrest. Taken together, our data suggest that heterogeneous methylation largely reflects asynchronous proliferation, but is intrinsic to actively engaged cis-regulatory elements and cancer.

Cytosine methylation represents a classic epigenetic modification that is faithfully transmitted over DNA replication by recognition of information retained on the parental strand. In mammals, its prevalence within the CpG dinucleotide context provides a symmetrical substrate to restore transiently hemimethylated states, an elegant mechanism that resembles the Watson–Crick model of genetic inheritance[1,2]. Three enzymes are generally responsible for establishing and maintaining this modification: DNA methyltransferases 1 (DNMT1), 3A (DNMT3A), and 3B (DNMT3B), all of which are essential for normal mammalian development[3]. Maintenance appears to be predominantly accomplished by DNMT1, which localizes to replication foci[4] and exhibits 10–40-fold higher binding affinity and catalytic activity toward hemimethylated DNA substrates[5–7]. DNMT1 is also recruited to nascent DNA by the essential cofactor UHRF1 (ubiquitin-like, with PHD and RING finger domains 1), which exhibits a high affinity for hemimethylated DNA through its SRA domain[8,9] and ubiquitinates the histone H3 tail to facilitate DNMT1 recruitment[10]. DNMT1 activity is further directed to the replication fork through its interaction with the proliferating cell nuclear antigen (PCNA) DNA clamp[11], and deletion of DNMT1's PCNA-binding domain has been reported to delay post-replication remethylation[12]. More conceptually, accurate re-establishment of the human methylome requires catalytic activity at ~45 million heterogeneously distributed CpGs (roughly 80% of CpG sites within the diploid genome) that must be completed within a single cell cycle[13]. Given this scale, it may not be surprising that some earlier studies have observed a lag in nascent strand methylation in somatic and transformed cells[14–18], which presumably reflects the kinetic discrepancy between rapid polymer extension from the 3′-OH of the previously incorporated base versus the multistep transfer of a methyl group to hemimethylated CpG dyads[19,20]. However, the global scale, kinetics and possible implications of this disconnect between copying genetic versus epigenetic information remain to be determined.

Results

Repli-BS identifies a global delay in methylation of nascent DNA. To investigate the acquisition of CpG methylation on nascent DNA, we combined immunoprecipitation of bromodeoxyuridine (BrdU)-labeled nascent strands followed by sequencing (Repli-seq)[21] with bisulfite treatment to measure post-replication cytosine methylation at base pair resolution (Repli-bisulfite seq: Repli-BS, Fig. 1a, Supplementary Fig. 1a and Methods). Human embryonic stem cells (ESCs; male HUES64) were treated for one hour with BrdU and sorted into six S-phase fractions (S1–S6) before BrdU immunoprecipitation followed by bisulfite sequencing (Fig. 1a,b, Supplementary Fig. 1b and Supplementary Dataset 1). We initially pooled data from the six fractions and compared the methylation level of ~24.5 million newly replicated (nascent) CpGs to bulk (non-sorted, no BrdU immunoprecipitation) whole-genome bisulfite sequencing (WGBS) data. Whereas our bulk reference population exhibited a canonical methylation landscape with high CpG methylation (mean of 0.83), the average for DNA synthesized within our 1-h BrdU pulse was globally reduced (mean 0.64; Fig. 1c and Supplementary Fig. 1c). This discrepancy was consistent across early (S1 + S2; mean of 0.63), mid (S3 + S4; mean of 0.63) and late (S5 + S6; mean of 0.66) S-phase stages (Supplementary Fig. 1d). Moreover, we found that different measured genomic features appeared equally affected by this delay, including promoters, enhancers and gene bodies, showing no correlation with gene expression level (Supplementary Fig. 1e,f). CpG density as well as enrichment for the Polycomb repressive complex 2 (PRC2) subunit EZH2 appeared to have some influence on a very small subset of CpGs (Supplementary Fig. 1g–j). We also observed a global delay for non-CpG methylation, which was more apparent for gene bodies,

[1]Department of Genome Regulation, Max Planck Institute for Molecular Genetics, Berlin, Germany. [2]Department of Stem Cell and Regenerative Biology, Harvard University, Cambridge, MA, USA. [3]Broad Institute of MIT and Harvard, Cambridge, MA, USA. [4]The Ken & Ruth Davee Department of Neurology, Department of Physiology, Feinberg School of Medicine, Northwestern University, Chicago, IL, USA. [5]Department of Translational Psychiatry, Max Planck Institute of Psychiatry, Munich, Germany. [6]Present address: Department of Biomedical Engineering, University of California-Irvine, Irvine, CA, USA. [7]These authors contributed equally: Jocelyn Charlton and Timothy L. Downing. *e-mail: meissner@molgen.mpg.de

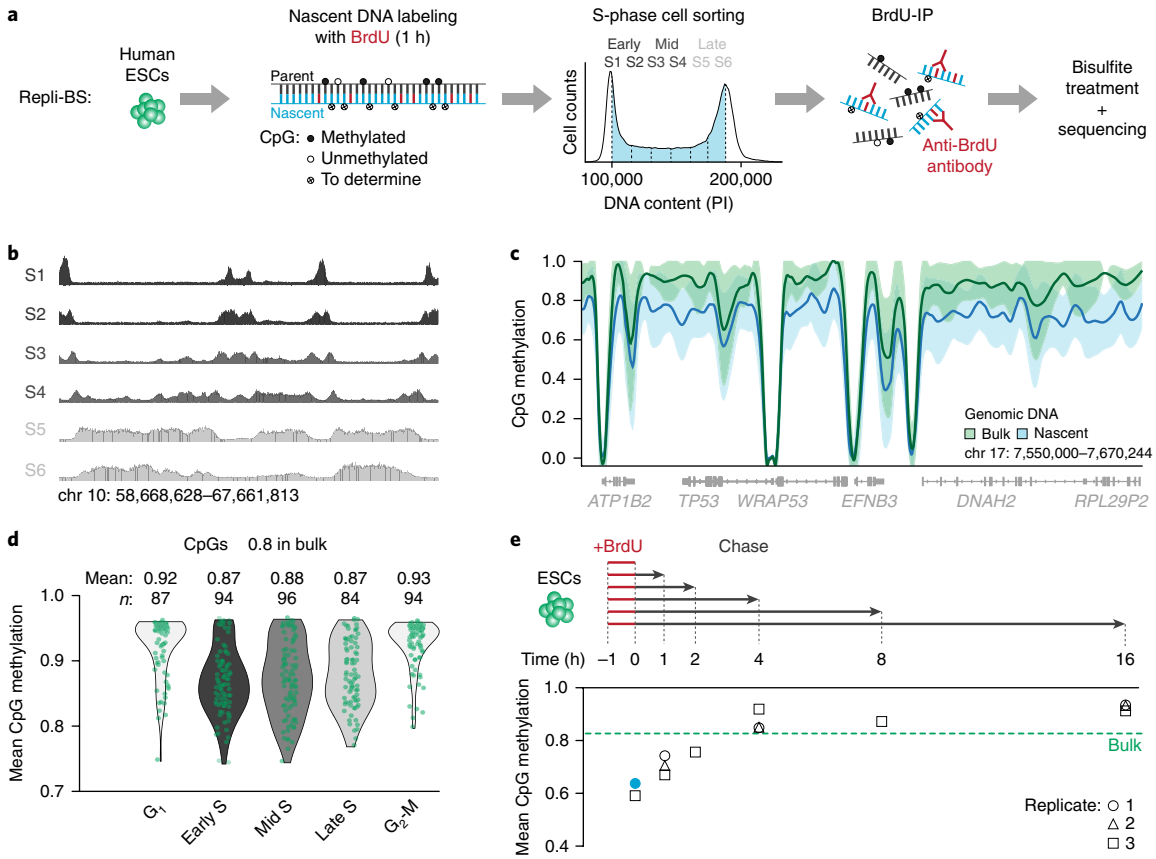

Fig. 1 | Repli-BS identifies a global delay in the acquisition of CpG methylation on nascent DNA. a, Schematic of our experimental design. Asynchronously growing human ESCs are labeled with BrdU for 1 h. During the pulse, BrdU (red) is incorporated into newly synthesized nascent DNA (blue) as it is copied from the parental strand (black). Empty circles marked with an 'x' ('to determine') indicate CpGs investigated by Repli-BS for methylation status. Six gates of equal proportion were used to sort S-phase cells according to DNA content. BrdU immunoprecipitation (BrdU-IP) was performed to capture newly replicated DNA strands, which were treated with bisulfite before library generation and sequencing. **b**, Genome browser tracks show read density and corresponding replication pattern across each of the six collected S-phase fractions. **c**, Local regression analysis was performed using methylation values for CpGs within nascent (S1–S6) and bulk genomic DNA. LOESS-smoothed mean methylation levels are displayed as bold lines. Shaded areas show one s.d. **d**, Single-cell RRBS data for cells sorted by cell cycle stage. Violin plots with overlaid strip plots display mean methylation per cell for all CpGs with methylation ≥0.8 in bulk cells. Each green dot represents one cell. Despite not isolating nascent DNA, 85% of S-phase cells ($n = 236$ of 274) display lower mean methylation levels than bulk ESCs. **e**, ESCs were pulsed with BrdU for 1 h, chased in normal growth medium for 1–16 h and analyzed by Repli-BS. Mean CpG methylation levels for nascent DNA samples are shown below. Dashed green line shows genomic average for bulk DNA. Nascent mean methylation after the initial labeling (0 h) from **a** is indicated with the blue dot and black circles, and triangles and squares show mean nascent methylation for three replicates (replicates 1 and 2, same cellular material but different IPs; replicate 3, different cellular material).

repetitive elements and other known DNMT3A and DNMT3B targets (Supplementary Fig. 1k,l). Notably, the emergence of nonsymmetric methylation on the nascent strand requires de novo activity, as the parental strand cannot serve as a template and hence follows an alternative mechanism. Finally, we used single-cell RNA sequencing to determine expression of key epigenetic regulators throughout the cell cycle (Supplementary Fig. 2a and Supplementary Dataset 2) and in parallel applied a new multiplexed single-cell reduced representation bisulfite sequencing (RRBS) approach to measure cytosine methylation across individual cells sorted by DNA content. Cells in S phase showed lower mean methylation values compared to cells in G_1 or G_2-M, which independently points toward a replication-associated reduction in methylation (Fig. 1d and Supplementary Fig. 2b,c).

Biphasic remethylation of nascent DNA. To better understand the kinetics with which nascent DNA restores methylation over time, we chased BrdU-pulsed cells for 1–16 h before performing Repli-BS (Fig. 1e and Supplementary Dataset 1). The most notable methylation increase occurred within the first hour following replication, which could be associated with active recruitment of DNMT1 to the replication fork, followed by a slower, incremental period that stabilized to bulk reference levels after ~4 h (Fig. 1e and Supplementary Fig. 2d). The delayed kinetics of the second phase could reflect a replication-uncoupled search for unevenly dispersed hemimethylated targets. These dynamics appear to affect the genome equally (Supplementary Fig. 2e); however, while the mean methylation and rate of increase were remarkably similar between replicates (Fig. 1e), methylation typically emerged on distinct CpGs (Supplementary Fig. 2f). This finding suggests that the temporal order of adding this modification is not genetically encoded and may instead be determined by the molecular limits of DNMT1 activity near the replication fork, where additional processes may act as obstructions. The gain of methylation over time can also be measured at single-molecule resolution by determining the read-level progression from partial to fully methylated states (Supplementary Fig. 2g,h), which confirmed a high correlation between neighboring CpGs that would be consistent with in vitro measurements reporting a processive activity for DNMT1 (refs [6,22]) (Supplementary Fig. 2i).

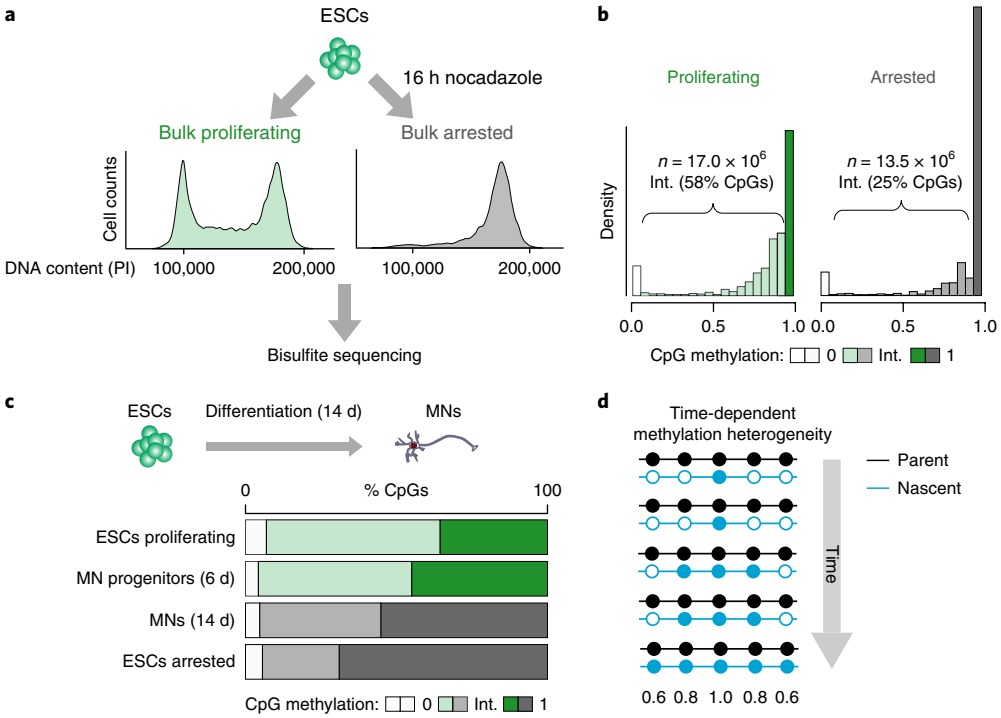

Fig. 2 | Mitotically arrested cells show reduced intermediate CpG methylation suggesting time-dependent methylation heterogeneity. a, ESCs were grown in either normal ('proliferating') culture conditions (green) or in the presence of the mitotic inhibitor nocodazole for 16 h ('arrested'; gray). The fluorescence-activated cell sorting (FACS) plots show representative histograms according to DNA content (propidium iodide (PI) intensity) for cells from each experimental condition, confirming the shift to G_2-M phase (4N) for nocodazole-treated cells (right). Genomic DNA was extracted from both conditions and bisulfite sequencing was performed. **b**, Histograms showing the distribution of CpG methylation in cells grown in proliferating and arrested conditions. Intermediate (int.) methylation (shown in intermediate shading) refers to CpGs with methylation levels other than 0 (light shading) or 1 (dark shading). **c**, ESCs were differentiated toward post-mitotic MNs, and samples on day 6 and 14 were analyzed by WGBS to determine the proportion of CpGs with intermediate methylation levels. **d**, Simplified schematic illustrating a hypothetical scenario of methylation heterogeneity arising from a lag in maintenance methylation following DNA synthesis. The gray arrow indicates time during S phase. In an unsynchronized population, cells exist in all stages of S phase, and, therefore, each displays different methylation levels with respect to 'time'. Nascent DNA is colored blue and is gradually methylated over time. Filled circle, methylated CpG; empty circle, unmethylated CpG. Numbers below indicate the expected mean methylation for the CpGs at that position based on the illustrated pattern.

DNMT3A and DNMT3B have a limited effect on post-replication methylation rate. As previously observed, genetic deletion of DNMT1 in mouse and human ESCs results in rapid, global loss of CpG methylation, thus confirming the central role of DNMT1 in methylation maintenance[23,24]. Long-term passaging of DNMT3A and DNMT3B double knockout (DKO) ESCs results in a gradual loss of methylation, showing that the de novo methyltransferases are required to compensate for the incomplete maintenance fidelity of DNMT1 (refs [24,25]). After approximately 20 passages, our human DKO cells showed a global decrease in CpG methylation of 10% (Supplementary Fig. 3a). To assess the contribution of the de novo DNMTs to post-replication nascent strand methylation, we repeated the 1-h BrdU pulse-chase Repli-BS experiment in the DKO cells and observed that DNMT1 is able to methylate nascent DNA to DKO bulk levels in the absence of any de novo activity (Supplementary Fig. 3b–d). In fact, the nascent strand methylation rate appeared slightly faster than that in wild-type cells, which may be caused by the reduced number of targets (hemimethylated CpGs) in the comparatively hypomethylated DKO line.

Distinct origins of global intermediate methylation. In both cell lines, our data show that the delay in methylation of nascent DNA reduces global methylation levels. Given that ~35% cells within an unsynchronized ESC population are undergoing replication at any given time, we hypothesized that the intrinsically lower global methylation of S-phase cells may contribute to the intermediate methylation (values other than 0% or 100%) observed in bulk measurements, which are often attributed to intercellular heterogeneity. To investigate this possibility, we arrested ESCs in prometaphase and performed WGBS to determine whether absence of cells in S phase reduces the fraction of intermediately methylated CpGs (Fig. 2a, Supplementary Fig. 4a,b and Supplementary Dataset 1), which comprise the majority (58%) of CpGs in proliferating ESCs (Fig. 2b). In line with our hypothesis, the number of unmethylated CpGs (with 0% methylation) remained roughly constant between proliferating and arrested cells (5.6 and 6.9%). In contrast, intermediately methylated CpG sites were reduced from 58% in proliferating cells to 25% in arrested cells, with a concomitant increase in the number of fully methylated CpGs from 36% to 69% (Fig. 2b and Supplementary Fig. 4c). This shift was independent of CpG coverage (Supplementary Fig. 4d) and was further validated by differentiating ESCs into post-mitotic spinal motor neurons (MNs)[26], which reduced the proportion of proliferating cells without artificial arrest (Fig. 2c). After two weeks, the majority (~90%) of differentiated cells were negative for proliferation marker Ki-67, and the proportion of intermediately methylated CpGs indeed decreased as predicted (Fig. 2c), which suggests that global methylation heterogeneity in ESCs arises largely as a byproduct of time-dependent nascent strand methylation (Fig. 2d). Of interest, intercellular DNA methylation heterogeneity has been frequently noted in cancer cells

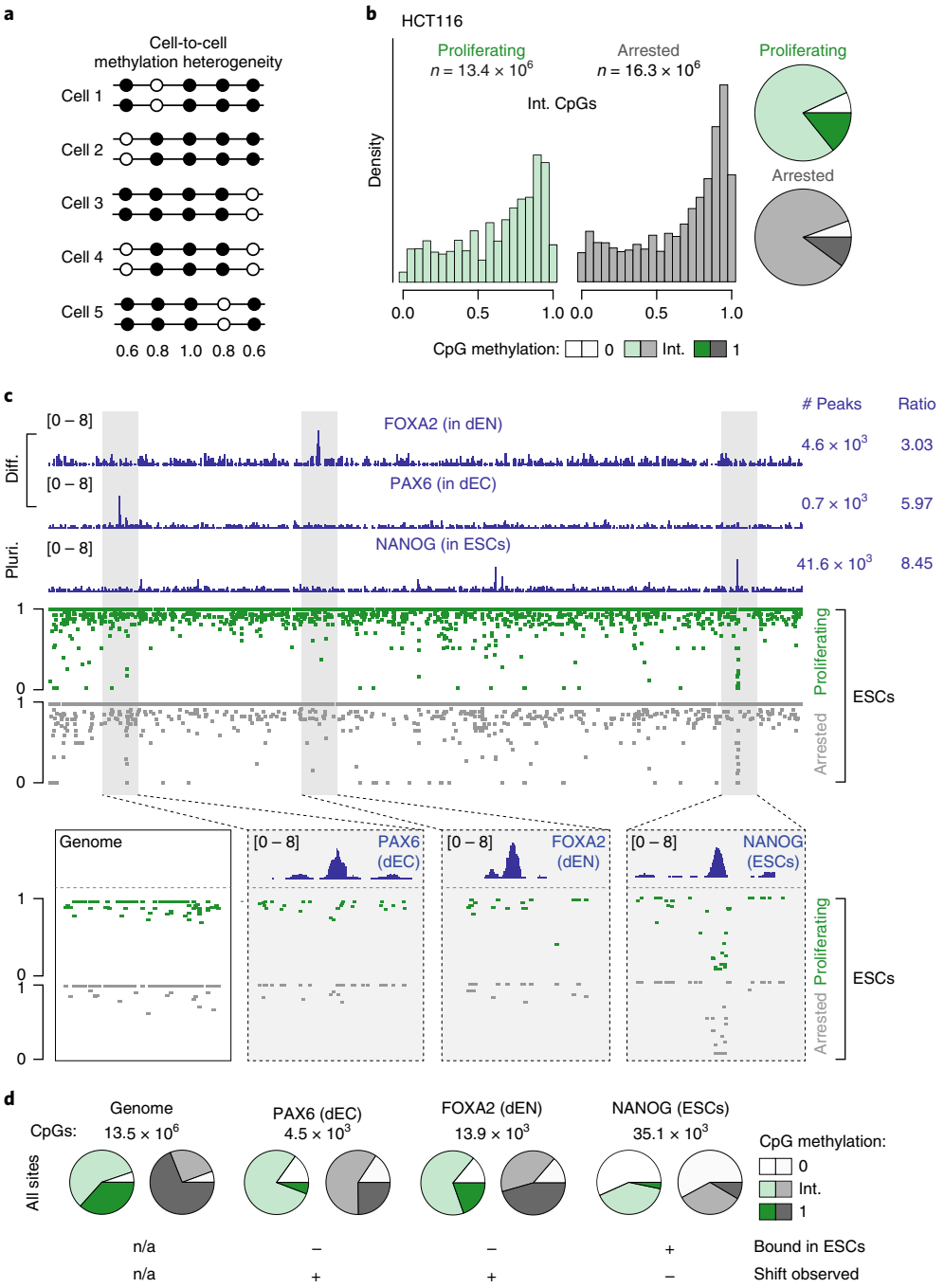

Fig. 3 | Cancer cells and active TF binding sites display inherent cell-to-cell methylation heterogeneity. a, Simplified schematic analogous to Fig. 2d, showing an alternative hypothetical scenario that represents CpG methylation heterogeneity arising from cell-to-cell differences. Filled circle, methylated CpG; empty circle, unmethylated CpG. Numbers below indicate the expected mean methylation for the CpGs at that position based on the illustrated pattern. **b**, Left, histograms displaying methylation levels for bulk and arrested CpGs with intermediate methylation in HCT116 cells. Right, pie charts summarizing the distribution of unmethylated, intermediate and fully methylated CpGs in proliferating and arrested HCT116 cells for CpGs covered at ≥ 15×. **c**, Top, ChIP-seq tracks (chr. 5: 163,394,518–163,756,719) for FOXA2 in ESCs differentiated for 5 d into endoderm (dEN), PAX6 in ESCs differentiated for 5 d into ectoderm (dEC) and NANOG in undifferentiated pluripotent ESCs. Diff., differentiated; pluri., pluripotent. Peaks indicate total number of peaks called by MACS2. Ratio is the average number of CpGs per peak. Middle, WGBS tracks for proliferating and arrested ESCs. For each TF, methylation levels in proliferating and arrested ESCs that show a shift to high methylation levels (as in the 'genome' example) for nonbound sites but no shift in the engaged NANOG binding site are shown. Genome, chr. 5: 163,477,070–163,491,961; PAX6, chr. 5: 163,434,313–163,439,131; FOXA2, chr. 5: 163,527,525–163,531,337; NANOG, chr. 5: 163,721,080–163,726,485. **d**, Global analysis of the phenomena described locally in **c**. When considering all CpGs or the ones found at not actively bound (but experimentally confirmed) TF binding sites, we observed a similar decrease in the percentage of CpGs with intermediate methylation levels (decrease of 33% for all CpGs, 22% for FOXA2 and 20% for PAX6; '+ shift observed'), whereas sites that are bound by NANOG in ESCs do not show this behavior and remain largely unchanged despite the arrest (decrease of only 4%; '– shift observed').

in association with reduced global methylation levels[27,28] (Fig. 3a). Considering our results, it seemed possible that the elevated fraction of intermediate methylation levels in cancer cells could be associated with the highly proliferative nature of these transformed cells. To explore this, we arrested the colon cancer cell line HCT116 and found an expected increase in mean methylation levels (from eliminating contribution of nascent strands with reduced methylation) but not a shift toward full methylation, as observed in ESCs (Fig. 3b and Supplementary Fig. 4e,f). Although we only investigate HCT116 cells here, our data suggest that the epigenetic heterogeneity in cancer cells is a combination of both replication-associated and elevated cell-to-cell variation.

Intermediate methylation at bound transcription factor targets points to intercellular heterogeneity. Prior studies have also suggested that intermediate levels of methylation are frequently found around transcription factor (TF) binding sites[13,29,30]. To compare these local events with the global patterns described above, we re-examined our bulk and arrested ESC datasets and used previously determined TF binding sites determined by chromatin immunoprecipitation followed by sequencing (ChIP-seq) experiments in ESCs as well as their differentiated derivatives. We first identified TF targets that are engaged and thus actively regulated in pluripotent cells (OCT4 or NANOG) as well as differentiation-specific target sites (PAX6 in ectoderm, FOXA2 in endoderm, GATA6 in mesoderm and EOMES in mesendoderm) that are not bound in undifferentiated ESCs and should therefore behave like the genomic average (Fig. 3c and Supplementary Fig. 4g,h). We then compared methylation levels for bulk and arrested ESCs and found that differentiation-specific regions behaved like the greater genome, whereas actively engaged sites preserved their intermediate methylation status. This finding suggests that TF binding may play a direct role in establishing local intercellular heterogeneity (Fig. 3c,d and Supplementary Fig. 4g,h).

Discussion

We applied a genome-wide approach to measure cytosine methylation levels of nascent DNA (Repli-BS) and found a persistent lag in the re-establishment of both CpG and non-CpG methylation following DNA synthesis. For CpG methylation, the rapid initial surge that we observed is consistent with replication fork-based DNMT1 recruitment via its PCNA-binding domain, which, when absent, reduces the nascent strand methylation rate [31]. It appears that the initial seeding of DNMT1 generally does not occur at fixed locations, as we were not able to identify commonly or disproportionately hypermethylated features in our pulse-chase experiment. Consecutive CpGs were methylated in the majority of nascent reads, supporting in vitro observations that suggest DNMT1 acts in a processive manner on the same molecule. However, the possibility cannot be excluded that DNMT1 may also methylate larger chromatin domains more rapidly through alternative modes of recruitment. In our DNMT3 DKO experiments, we made the intriguing observation that reduced global methylation levels appear to increase the nascent strand methylation rate. In the future, it will be interesting to further explore how substrate (hemimethylated targets) and enzyme (DNMT1) levels affect the kinetics of post-replication methylation and whether this enzyme/substrate ratio can be mechanistically linked to the reduced, but generally stable, levels of global methylation across cancer types[32–34]. In this context, we show that intermediate methylation in cancer cells arises as a result of both inherent intercellular epigenetic heterogeneity and cell-cycle-linked heterogeneity. In contrast, the extensive methylation maintenance lag in human ESCs is largely explained by the fraction of cells in S phase. We expect that the emerging insights from our study may allow for more precise analysis of regions that display true intermediate methylation values in nontransformed cells and will improve their biological interpretation. Finally, it remains to be determined whether the global lag in epigenetic transmission following replication has a functional role at some sites including, but not limited to, providing a window of opportunity for TF binding during coordinated cell state transitions[35]. A similar mechanism has recently been reported for H3K27me3 (ref. [36]). In conclusion, our description of the genome-wide lag between the copying of genetic and epigenetic information adds further insight to our understanding of how epigenetic information is mitotically inherited.

Methods

Methods, including statements of data availability and any associated accession codes and references, are available at https://doi.org/10.1038/s41594-018-0046-4.

Received: 18 October 2017; Accepted: 5 February 2018;
Published online: 12 March 2018

References

1. Holliday, R. & Pugh, J. E. DNA modification mechanisms and gene activity during development. *Science* **187**, 226–232 (1975).
2. Riggs, A. D. X inactivation, differentiation, and DNA methylation. *Cytogenet. Cell. Genet.* **14**, 9–25 (1975).
3. Smith, Z. D. & Meissner, A. DNA methylation: roles in mammalian development. *Nat. Rev. Genet.* **14**, 204–220 (2013).
4. Prelich, G. & Stillman, B. Coordinated leading and lagging strand synthesis during SV40 DNA replication in vitro requires PCNA. *Cell* **53**, 117–126 (1988).
5. Bestor, T. H. & Ingram, V. M. Two DNA methyltransferases from murine erythroleukemia cells: purification, sequence specificity, and mode of interaction with DNA. *Proc. Natl Acad. Sci. USA* **80**, 5559–5563 (1983).
6. Hermann, A., Goyal, R. & Jeltsch, A. The Dnmt1 DNA-(cytosine-C5)-methyltransferase methylates DNA processively with high preference for hemimethylated target sites. *J. Biol. Chem.* **279**, 48350–48359 (2004).
7. Pradhan, S. et al. Baculovirus-mediated expression and characterization of the full-length murine DNA methyltransferase. *Nucleic. Acids. Res.* **25**, 4666–4673 (1997).
8. Bostick, M. et al. UHRF1 plays a role in maintaining DNA methylation in mammalian cells. *Science* **317**, 1760–1764 (2007).
9. Sharif, J. et al. The SRA protein Np95 mediates epigenetic inheritance by recruiting Dnmt1 to methylated DNA. *Nature* **450**, 908–912 (2007).
10. Qin, W. et al. DNA methylation requires a DNMT1 ubiquitin interacting motif (UIM) and histone ubiquitination. *Cell. Res.* **25**, 911–929 (2015).
11. Chuang, L. S. et al. Human DNA-(cytosine-5) methyltransferase-PCNA complex as a target for p21WAF1. *Science* **277**, 1996–2000 (1997).
12. Schermelleh, L. et al. Dynamics of Dnmt1 interaction with the replication machinery and its role in postreplicative maintenance of DNA methylation. *Nucleic. Acids. Res.* **35**, 4301–4312 (2007).
13. Ziller, M. J. et al. Charting a dynamic DNA methylation landscape of the human genome. *Nature* **500**, 477–481 (2013).
14. Adams, R. L. The relationship between synthesis and methylation of DNA in mouse fibroblasts. *Biochim. Biophys. Acta.* **254**, 205–212 (1971).
15. Liang, G. et al. Cooperativity between DNA methyltransferases in the maintenance methylation of repetitive elements. *Mol. Cell. Biol.* **22**, 480–491 (2002).
16. Woodcock, D. M., Adams, J. K. & Cooper, I. A. Characteristics of enzymatic DNA methylation in cultured cells of human and hamster origin, and the effect of DNA replication inhibition. *Biochim. Biophys. Acta.* **696**, 15–22 (1982).
17. Woodcock, D. M. et al. Delayed DNA methylation is an integral feature of DNA replication in mammalian cells. *Exp. Cell. Res.* **166**, 103–112 (1986).
18. Shirodkar, A. V. et al. A mechanistic role for DNA methylation in endothelial cell aECa-enriched gene expression: relationship with DNA replication timing. *Blood* **121**, 3531–3540 (2013).
19. Jackson, D. A. & Pombo, A. Replicon clusters are stable units of chromosome structure: evidence that nuclear organization contributes to the efficient activation and propagation of S phase in human cells. *J. Cell. Biol.* **140**, 1285–1295 (1998).
20. Pradhan, S., Bacolla, A., Wells, R. D. & Roberts, R. J. Recombinant human DNA (cytosine-5) methyltransferase. I. Expression, purification, and comparison of de novo and maintenance methylation. *J. Biol. Chem.* **274**, 33002–33010 (1999).
21. Hansen, R. S. et al. Sequencing newly replicated DNA reveals widespread plasticity in human replication timing. *Proc. Natl Acad. Sci. USA* **107**, 139–144 (2010).

22. Jeltsch, A. & Jurkowska, R. Z. New concepts in DNA methylation. *Trends. Biochem. Sci.* **39**, 310–318 (2014).
23. Lei, H. et al. De novo DNA cytosine methyltransferase activities in mouse embryonic stem cells. *Development* **122**, 3195–3205 (1996).
24. Liao, J. et al. Targeted disruption of DNMT1, DNMT3A and DNMT3B in human embryonic stem cells. *Nat. Genet.* **47**, 469–478 (2015).
25. Jackson, M. et al. Severe global DNA hypomethylation blocks differentiation and induces histone hyperacetylation in embryonic stem cells. *Mol. Cell. Biol.* **24**, 8862–8871 (2004).
26. Ziller, M. J. et al. Dissecting the functional consequences of de novo DNA methylation dynamics in human motor neuron differentiation and physiology. *Cell Stem Cell* (in the press).
27. Hansen, K. D. et al. Increased methylation variation in epigenetic domains across cancer types. *Nat. Genet.* **43**, 768–775 (2011).
28. Landau, D. A. et al. Locally disordered methylation forms the basis of intratumor methylome variation in chronic lymphocytic leukemia. *Cancer Cell* **26**, 813–825 (2014).
29. Stadler, M. B. et al. DNA-binding factors shape the mouse methylome at distal regulatory regions. *Nature* **480**, 490–495, https://doi.org/10.1038/nature10716 (2011).
30. Elliott, G. et al. Intermediate DNA methylation is a conserved signature of genome regulation. *Nat. Commun.* **6**, 6363 (2015).
31. Liu, Y., Oakeley, E. J., Sun, L. & Jost, J. P. Multiple domains are involved in the targeting of the mouse DNA methyltransferase to the DNA replication foci. *Nucleic. Acids. Res.* **26**, 1038–1045 (1998).
32. Jones, P. A. & Baylin, S. B. The epigenomics of cancer. *Cell* **128**, 683–692 (2007).
33. Smith, Z. D. et al. Epigenetic restriction of extraembryonic lineages mirrors the somatic transition to cancer. *Nature* **549**, 543–547 (2017).
34. Witte, T., Plass, C. & Gerhauser, C. Pan-cancer patterns of DNA methylation. *Genome Med.* **6**, 66 (2014).
35. Donaghey, J. et al. Genetic determinants and epigenetic effects of pioneer-factor occupancy. *Nat. Genet.* **50**, 250–258 (2018).
36. Petruk, S. et al. Delayed accumulation of H3K27me3 on nascent DNA is essential for recruitment of transcription factors at early stages of stem cell differentiation. *Mol. Cell* **66**, 247–257.e245 (2017).

Acknowledgements

We thank all members of the Meissner laboratory and in particular R. Karnik. We also thank A. Jeltsch for providing thoughtful feedback on the manuscript. T.L.D. was supported in part by postdoctoral fellowships from the Ford Foundation, UNCF/Merck Science Initiative, Harvard Medical School, and the Broad Institute Diversity Initiative. The Kiskinis lab gratefully acknowledges financial support from the Les Turner ALS Foundation, Muscular Dystrophy Association and the Feinberg School of Medicine. A.M. is a New York Stem Cell Foundation – Robertson Investigator. The Max Planck Society, the New York Stem Cell Foundation, the Broad Institute (SPARC funding to develop single cell RRBS) and NIH grants (1P50HG006193, P01GM099117, R01DA036898) supported this work.

Author contributions

J.C., T.L.D. and A.M. designed the study with input from Z.D.S. T.L.D., J.C., R.P. and V.A. performed the experiments. H.G. and A.G. developed the multiplexed single-cell RRBS protocol, generated the sequencing libraries and helped with experimental design and analysis. K.C., S.K., B.T. and M.J.Z. assisted in data processing. J.C. performed bioinformatics analyses. A.M.T. performed the single-cell RNA-seq cell cycle analysis. D.P.S. and E.K. performed the MN differentiation, characterization and sample collection. J.C., T.L.D., Z.D.S., A.G. and A.M. interpreted the data. J.C., T.L.D., Z.D.S. and A.M. wrote the manuscript with assistance from the other authors.

Competing interests

The authors declare no competing interests.

Additional information

Supplementary information is available for this paper at https://doi.org/10.1038/s41594-018-0046-4.

Reprints and permissions information is available at www.nature.com/reprints.

Correspondence and requests for materials should be addressed to A.M.

Publisher's note: Springer Nature remains neutral with regard to jurisdictional claims in published maps and institutional affiliations.

Methods

Cell culture. Human embryonic stem cells (male HUES64; obtained from Harvard University) and the modified variant DNMT3A$^{-/-}$DNMT3B$^{-/-}$ (HUES64 DKO) cells were grown in feeder-free conditions using Geltrex (Thermo Fisher Scientific) and mTeSR (STEMCELL Technologies). HCT116 cells (obtained from S. B. Baylin at the Sidney Kimmel Comprehensive Cancer Center at Johns Hopkins) were grown in McCoy's 5A (modified) medium supplemented with 10% FBS and 1% penicillin and streptomycin. All cell lines tested negative for mycoplasma.

Bulk versus arrested population measurements. Cells were either grown with no treatment (bulk) or arrested using 2 µg/ml nocodazole for 16 h, then collected and washed twice with PBS. Arrested cells were stained using the live-dead Fixable Blue Dead Cell Stain kit (Thermo Fisher Scientific) according to manufacturer's recommendations, then fixed by adding 100% ethanol dropwise to the cell suspension until a final ethanol concentration of 75% was achieved. Fixed arrested cells were then counterstained with propidium iodide (PI) before FACS sorting to collect cells in G_2-M phase.

BrdU treatment. To label nascent strands of DNA, BrdU (5-bromo-2′-deoxyuridine; BD Biosciences) was added to cell culture medium at a final concentration of 50 µM. Cells were incubated for 1 h at 37 °C to allow incorporation of BrdU nucleotides into newly synthesized DNA. Cells were washed three times with basal media (DMEM-F12), then either collected immediately or incubated at 37 °C for the duration of the chase before collection. To collect, cells were detached from tissue culture plates and disaggregated into single cells using StemPro Accutase Cell Dissociation Reagent (Thermo Fisher Scientific) for ESCs and 0.05% trypsin for HCT116. Cells were then pelleted, resuspended in PBS and either fixed in ethanol as described above or snap frozen.

Enrichment for BrdU-labeled DNA (original). Genomic DNA was isolated by incubating cells in SDS-PK buffer (0.5% wt/vol) sodium dodecyl sulfate (SDS), 50 mM Tris-HCl, 0.01 M EDTA, 1 M NaCl and 0.2 mg/ml proteinase K) at 56 °C for 2 h. Phenol-chloroform extraction was performed, and genomic DNA was precipitated in one volume of isopropanol at −20 °C. DNA was pelleted, washed with ethanol and resuspended in TE buffer. Genomic DNA was fragmented to an average size of 200 bp using a Branson Digital Sonifier (Model 250) and a Branson 101-148-063 microtip. DNA was sonicated using 40% amplitude for a total of 4 min. A double-antibody immunoprecipitation was performed to isolate nascent (BrdU labeled) strands of DNA. For each immunoprecipitation reaction, at least 120 ng of sonicated DNA was used. DNA was first heat denatured at 95 °C for 5 min and rapidly cooled on ice. 12.5 µg primary antibody (mouse anti-BrdU, BD Biosciences Pharmingen) was added to the ssDNA suspension with constant rocking for 20 min and then 20 µg of secondary antibody (rabbit anti-mouse IgG, Sigma, cat. no. M-7023) was added and stained for 20 min. Antibody–DNA complexes were then pelleted, resuspended and incubated in digestion buffer (50 mM Tris-HCl, 0.01 M EDTA, 0.5% SDS and 0.25 mg/ml proteinase K) at 37 °C overnight. Nascent ssDNA was subsequently purified by phenol-chloroform extraction and ethanol precipitation.

Enrichment for BrdU-labeled DNA (optimized). The above protocol was adapted to decrease the length of sample processing specifically for non-fixed, non-sorted cells. DNA was isolated using the Quick-DNA Universal kit (Zymo Research). Sonication was performed at 40% amplitude for 2 min for samples resuspended in 200 µl, 4 min for samples resuspended in 500 µl or in a 96-well plate using a Covaris 96-well sonicator (E220) for 75 s per sample. BrdU immunoprecipitation was performed for 60 min and 30 min for primary and secondary antibodies listed above, respectively, and then nascent ssDNA was purified using the Agencourt AMPure XP system (Beckman Coulter).

FACS and cell cycle analysis. Fixed cells, (in some cases BrdU labeled and/or with live-dead stain) were pelleted and washed twice in FACS buffer (1% FBS in PBS) and then stained with PI for 20–30 min. Cells were also coincubated with RNase A (0.250 mg/ml). Prior to sorting, cells were passed through 40 µm filter FACS tubes. FACS was performed using a BD FACS Aria Cell Sorter with a 100 µm nozzle under low pressure. To identify G_1, S and G_2-M cell populations, three sequential gating strategies were applied to the bulk sample population. Cell debris were removed using a forward versus side scatter comparison, dead cells were removed based on live-dead Fixable Blue stain intensity, and, finally, single cells (singlets) were enriched using a PI signal width versus height comparison strategy.

Motor neuron differentiation. Human ESC colonies were dissociated using Accutase and plated at a density of 74,000 cells/cm^2 with 10 µM ROCK inhibitor (Y-27632, DNSK International) in mTeSR1 for 48 h. Media was replaced on day 0 with N2B27 medium (50% DMEM:F12, 50% Neurobasal, supplemented with NEAA, Glutamax, N2 and B27; Gibco, Life Technologies) containing 10 µM SB431542 (DNSK International), 100 nM LDN-193189 (DNSK International), 1 µM retinoic acid (RA, Sigma) and 1 µM of smoothened agonist (SAG, DNSK International). Culture medium was changed daily for 6 d and was then switched to N2B27 medium supplemented with 1 µM RA, 1 µM SAG, 5 µM DAPT (DNSK International) and 4 µM SU5402 (DNSK International). Cells were fed daily until day 14 of differentiation. At day 6 and 14, cells were collected for WGBS.

Multiplexed single-cell RRBS. ESCs were collected, fixed in 75% ethanol and stained with PI. Cells were then sorted by cell cycle phase into G_1, early S, mid S, late S and G_2-M phase to obtain one cell per well in a 96-well plate containing 5 µl 0.1× CutSmart buffer (New England BioLabs) per well (480 cells total). Sorted cells were lysed at 50 °C for 2 h in a reaction containing 0.2 U proteinase K (New England Biolabs), 0.2% Triton X-100 (EMD Millipore) and 1× CutSmart buffer. After heat-inactivation of proteinase K at 75 °C for 30 min, we added 2 µl of digestion buffer consisting of 1× CutSmart buffer and 0.5 µl MspI (20 U/µl, New England Biolabs) directly to each cell lysis reaction. The digested DNA was end-repaired and adenylated by adding 2 µl of a mixture containing 2.5 U Klenow fragment (3′-5′exo-, NEB), 0.4 µl of dNTP mixture (10 mM dATP, 1 mM dCTP and 1 mM dGTP) and 1 × CutSmart buffer to each sample and incubating at 30 °C for 25 min, then at 37 °C for another 30 min. After heat inactivation at 70 °C for 10 min, adenylated DNA fragments were ligated with 5 mC substituted indexed adapters overnight at 16 °C through distributing to each well 3 µl of reaction containing 800 U of T4 ligase (NEB), 0.1 µl of 100 mM ATP (Roche), 1.5 µl of 0.1 µM methylated indexed adaptor and 1× CutSmart buffer. 24 indexed ligation reactions were pooled, purified on AmPure XP beads and subjected to sodium bisulfite treatment using an EpiTect Fast Bisulfite kit (QIAGEN) following the manufacturer's recommendations with extended conversion time (20 min each cycle). The bisulfite converted multiplex RRBS library was amplified for a total of 18 cycles using KAPA HiFi Uracil + DNA Polymerase. The PCR program consisted of 98 °C denaturation for 45 s, six cycles of 98 °C for 20 s, 58 °C annealing for 30 s and 72 °C extension for 1 min, followed by 12 cycles of 98 °C for 20 s, 65 °C annealing for 30 s and 72 °C extension for 1 min and a final extension for 72 °C for 5 min. Pooled multiplex RRBS libraries with a size range of 150–700 bp were size selected and gel purified to remove adaptor dimers before being loaded onto an Illumina HiSeq2500 sequencer. We performed paired-end sequencing runs for a total of 200 cycles. In total, only 25 out of 480 cells failed to generate sufficient reads for further analysis.

Single-cell RNA-seq. Two 96-well plates of human ES and mesoderm single cells were used to make libraries for single-cell RNA-sequencing. Library generation and analysis was done as described in ref. [37]. Briefly, RNA-seq reads were first trimmed using Trimmomatic[38]. Trimmed reads were aligned to the RefSeq hg38 genome and transcriptome (GRCh38.2) using Bowtie2 (ref. [39]) and TopHat[40], respectively. The resulting transcriptome alignments were processed by RSEM to estimate the abundance of RefSeq transcripts, in transcripts per kilobase million (TPM). All cells with less than 4,000 detectable annotated transcripts were removed from further analysis. Detectable transcripts were defined as transcripts with TPM > 1. After removing apoptotic cells and background differentiation, we ordered cells according to progress in the cell cycle, as done previously[41]. Expression values displayed in Supplementary Fig. 2a were averaged using a moving window of 20 cells.

Quantifying gene expression cycling in G_1-S and S phase. We ordered all G_1-S and S-phase cells according to progress along the cell cycle, found the 20-cell window with highest and lowest expression for each gene and calculated a *t* test *P* value. We then permuted the order of all G_1-S and S-phase cells at random and calculated the highest and lowest expression 20-cell windows for each gene and corresponding control *t* test *P* value. A false discovery rate (FDR) of finding a gene with a treatment *P* value was measured by counting the number of genes with a more significant *P* value in the control experiment with permuted cell order normalized to the total number of control gene experiments. Genes were ranked in their cycling of expression using the FDR measure, ordering from smallest to largest.

Bisulfite sequencing. Either total genomic DNA (for WGBS) or DNA fragments recovered from the BrdU antibody pulldown (for Repli-BS) was concentrated by ethanol precipitation (final volume 20 µl). For the motor neuron samples, genomic DNA was fragmented using a Covaris S2 for 6 min according to the following program: duty cycle 5%; intensity 10; cycle per burst 200. The sheared DNA was purified using the DNA Clean & Concentrator kit from Zymo Research per the manufacturer's recommendations. For all samples, bisulfite conversion was carried out using the Zymo DNA Methylation-Gold Kit according to the manufacturer's instructions, and the bisulfite-converted DNA was recovered with 15 µl elution buffer. The eluted DNA was processed immediately using the Accel-NGS Methyl-seq DNA library kit (Swift Biosciences) following the manufacturer's recommendations with slight modifications. Specifically, we optimized the PCR cycle number required for library DNA enrichments by performing a range of PCR cycles (10, 12, 14, and 16) using 10% of the post-ligation DNA. The minimal cycle number was then used for the sample PCR to generate the sequencing libraries. PCR products were cleaned up using the Agencourt AMPure XP system (Beckman Coulter), and the final library DNA was eluted in 12 µl elution buffer. Using the Agilent Bioanalyzer we confirmed the absence of adaptor–dimers. If residual traces were detected, we performed an agarose gel size-selection to further clean up the final library. Up to 12 indexed sequencing libraries were pooled together for

sequencing using a 100-cycle paired-end (PE) run on an Illumina HiSeq 2500 or HiSeq 4000. For six nascent wild-type ESC time course samples (replicate 1, Fig. 1e), 75 base paired-end sequencing was performed.

Data processing and analysis. Raw sequencing reads were aligned against human genome version hg19/GRCh37 using BSMAP[42]. Custom Perl scripts were used to remove read pairs that aligned to different chromosomes. Paired-end read alignments rates varied between 71–94%, mean = 86% (Supplementary Dataset 1). Methylation calls were made by comparing the sequenced reads to the reference genome using custom Perl scripts. Unless otherwise indicated, only CpGs with a minimum coverage of ≥5× were used for the downstream analysis.

For comparison between nascent and bulk methylation levels, methylation ratios were generated by dividing the mean level of methylation for all nascent CpGs by the mean level of methylation for matched bulk CpGs. For non-CpGs, cytosine methylation levels were generated using BSMAP. To visualize read enrichment, IGV was used, and maximum coverage values were set to 20 for all tracks (scaled by 1,000,000 per total number of mapped reads). CpG density was calculated as the percentage of CpG dinucleotides per 100 bp.

To identify replication-timing domains specific to each S-phase fraction (S1–S6), we used a 10-kb sliding window to identify regions in which the average read density was 1.5× greater than the genomic average within each fraction. For the methylation analysis in Supplementary Figs. 1d and 2e, regions from S1 and S2, S3 and S4, and S5 and S6 fractions were merged and termed early, mid, and late fractions, respectively.

For genome methylation plots, LOESS smoothing and s.d. calculations were derived using the msir package in R (V1.3.1) with span set to 0.04 for the 120-kb region on chromosome 17 and 0.1 for the *POU5F1* (*OCT4*) locus. All genomic regions displayed are euchromatic. Violin plots were created using the R package 'vioplot' using standard parameters. Boxplots and heat maps in supplementary data were created using R. For boxplots, the median is shown in bold, the box displays interquartile range and whiskers extend to the most extreme data point that is no more than 1.5× the interquartile range.

For analysis of single-cell RRBS data, only CpGs that had methylation ≥0.8 in the ESC bulk sample were used to study methylation levels in single cells. This was done because RRBS captures predominantly regions with high CpG density, which are typically lowly methylated CpGs.

When comparing replicates, we confirmed the absence of coverage-dependent effects by comparing methylation of matched CpGs with ≥10× coverage in both samples. For the time course heat maps, only CpGs with ≥5× coverage in the combined replicate dataset and with ≥5× coverage in the bulk dataset were included.

For the genomic feature comparisons, CpGs from nascent or bulk DNA were intersected using BedTools v2.25.0 with: CpG islands, as previously defined in ref. [43], H1-specific typical or superenhancers, exons, introns, high CpG density or low CpG density promoters (ref. [44]), long interspersed nuclear elements (LINEs) and short interspersed nuclear elements (SINEs) downloaded from the UCSC Genome Browser. H3K27me3, H3K4me3, H3K27ac and EZH2 annotations were downloaded for H1 ESCs from UCSC. CpG density was calculated for 100-bp tiles as the total number of CpG dinucleotides per 100 bp.

To compare methylation levels between gene bodies of expressed versus non-expressed genes, bulk RNA-seq data were used from Gifford et al.[45]. Genes were binned into not expressed (FPKM < 1), expressed (FPKM > 10) and highly expressed (FPKM > 100). For all three categories, CpGs within gene bodies (using the UCSC RefSeq gene annotation) of the respective genes were taken, and nascent and bulk DNA methylation levels were compared.

For individual read analyses, we first extracted individual methylation read patterns using custom scripts written in Perl and applied custom R scripts to determine the CpG methylation status of consecutive sites for each read. Only reads with a minimum of three CpGs were considered for this analysis.

To account for differential coverage among samples (for example, arrested and bulk methylation levels; Supplementary Dataset 1), we downsampled the higher coverage sample to match the number of aligned reads in the comparison set. Specifically, for the arrested to bulk comparison, 28.5% of reads within the ESC bulk DNA dataset were selected at random, and methylation ratios were called as described above.

To investigate CpG methylation within transcription factor binding sites we used our previously described TF ChIP peak sets in human ESCs and their derivative germ cell layers (GSE61475): NANOG (ESC; GSM1505698), OCT4 (ESC; GSM1505724), FOXA2 (endoderm; GSM1505639), EOMES (mesendoderm; GSM1505630), GATA6 (mesoderm; GSM1505661) and PAX6 (Ectoderm; GSM1505715). Bulk and arrested datasets were intersected with the peak sets to obtain only CpGs located within TF binding sites. The proportion of CpGs that were equal to 0, 1 or intermediate was then calculated in bulk and arrested conditions. We repeated this analysis for only CpGs covered with at least ten reads and confirmed no coverage-dependent effects.

Life Sciences Reporting Summary. Further information on experimental design is available in the Life Sciences Reporting Summary.

Data availability. Data have been deposited in the Gene Expression Omnibus (GEO) under accession GSE82045. Other published datasets used in this study include: HUES64 (GSM1112841), HUES64 DNMT3A and DNMT3B DKO (GSM1545007), TF binding data (GSE61475) and motor neuron WGBS data (GSM2406773, MN-d6, and GSM2406772, MN-d14). Other data that support the findings of this study are available from the corresponding author upon reasonable request.

References

37. Trombetta, J. J. et al. Preparation of single-cell RNA-seq libraries for next generation sequencing. *Curr. Protoc. Mol. Biol.* **107**, 4.22.1–4.22.17 (2014).
38. Bolger, A. M., Lohse, M. & Usadel, B. Trimmomatic: a flexible trimmer for Illumina sequence data. *Bioinformatics.* **30**, 2114–2120 (2014).
39. Langmead, B. & Salzberg, S. L. Fast gapped-read alignment with Bowtie 2. *Nat. Methods* **9**, 357–359 (2012).
40. Trapnell, C., Pachter, L. & Salzberg, S. L. TopHat: discovering splice junctions with RNA-Seq. *Bioinformatics.* **25**, 1105–1111 (2009).
41. Kowalczyk, M. S. et al. Single-cell RNA-seq reveals changes in cell cycle and differentiation programs upon aging of hematopoietic stem cells. *Genome Res.* **25**, 1860–1872 (2015).
42. Xi, Y. & Li, W. BSMAP: whole genome bisulfite sequence MAPping program. *BMC Bioinformatics* **10**, 232 (2009).
43. Illingworth, R. et al. A novel CpG island set identifies tissue-specific methylation at developmental gene loci. *PLoS Biol.* **6**, e22 (2008).
44. Saxonov, S., Berg, P. & Brutlag, D. L. A genome-wide analysis of CpG dinucleotides in the human genome distinguishes two distinct classes of promoters. *Proc. Natl Acad. Sci. USA* **103**, 1412–1417 (2006).
45. Gifford, C. A. et al. Transcriptional and epigenetic dynamics during specification of human embryonic stem cells. *Cell* **153**, 1149–1163 (2013).

nature research

Corresponding author(s): Alexander Meissner

Life Sciences Reporting Summary

Nature Research wishes to improve the reproducibility of the work that we publish. This form is intended for publication with all accepted life science papers and provides structure for consistency and transparency in reporting. Every life science submission will use this form; some list items might not apply to an individual manuscript, but all fields must be completed for clarity.

For further information on the points included in this form, see Reporting Life Sciences Research. For further information on Nature Research policies, including our data availability policy, see Authors & Referees and the Editorial Policy Checklist.

Please do not complete any field with "not applicable" or n/a. Refer to the help text for what text to use if an item is not relevant to your study.
For final submission: please carefully check your responses for accuracy; you will not be able to make changes later.

Experimental design

1. Sample size

Describe how sample size was determined.

Our study did not require sample size determination and is based on sequencing measurements of cell populations.

2. Data exclusions

Describe any data exclusions.

No data was excluded.

3. Replication

Describe the measures taken to verify the reproducibility of the experimental findings.

We replicated our BrdU pulse-chase experiment in WT human ESCs three times with reproducible outcome.

4. Randomization

Describe how samples/organisms/participants were allocated into experimental groups.

There was no randomization required in this study.

5. Blinding

Describe whether the investigators were blinded to group allocation during data collection and/or analysis.

Blinding was not required.

Note: all in vivo studies must report how sample size was determined and whether blinding and randomization were used.

6. Statistical parameters

For all figures and tables that use statistical methods, confirm that the following items are present in relevant figure legends (or in the Methods section if additional space is needed).

n/a	Confirmed
☐	☒ The exact sample size (*n*) for each experimental group/condition, given as a discrete number and unit of measurement (animals, litters, cultures, etc.)
☐	☒ A description of how samples were collected, noting whether measurements were taken from distinct samples or whether the same sample was measured repeatedly
☐	☒ A statement indicating how many times each experiment was replicated
☐	☒ The statistical test(s) used and whether they are one- or two-sided *Only common tests should be described solely by name; describe more complex techniques in the Methods section.*
☐	☒ A description of any assumptions or corrections, such as an adjustment for multiple comparisons
☐	☒ Test values indicating whether an effect is present *Provide confidence intervals or give results of significance tests (e.g. P values) as exact values whenever appropriate and with effect sizes noted.*
☐	☒ A clear description of statistics including central tendency (e.g. median, mean) and variation (e.g. standard deviation, interquartile range)
☐	☒ Clearly defined error bars in all relevant figure captions (with explicit mention of central tendency and variation)

See the web collection on statistics for biologists for further resources and guidance.

Software

Policy information about availability of computer code

7. Software

Describe the software used to analyze the data in this study.	IGV was used to visualize data. Tools for data analysis are described in the methods section with the appropriate reference.

For manuscripts utilizing custom algorithms or software that are central to the paper but not yet described in the published literature, software must be made available to editors and reviewers upon request. We strongly encourage code deposition in a community repository (e.g. GitHub). *Nature Methods* guidance for providing algorithms and software for publication provides further information on this topic.

Materials and reagents

Policy information about availability of materials

8. Materials availability

Indicate whether there are restrictions on availability of unique materials or if these materials are only available for distribution by a third party.	There are no restrictions, material available upon request.

9. Antibodies

Describe the antibodies used and how they were validated for use in the system under study (i.e. assay and species).	Two antibodies were used for the BrdU immunoprecipitation: 1. mouse anti-BrdU, BD Biosciences Pharmingen, cat. no. 555627 2. rabbit anti-mouse IgG, Sigma, cat. no. M-7023

10. Eukaryotic cell lines

a. State the source of each eukaryotic cell line used.	HUES64 (Harvard University) HCT116 (Stephen Baylin)
b. Describe the method of cell line authentication used.	Trusted sources of the cell lines were used, all data matched the expectations for the respective cell lines. No additional authentication was performed.
c. Report whether the cell lines were tested for mycoplasma contamination.	All cell lines tested negative for mycoplasma.
d. If any of the cell lines used are listed in the database of commonly misidentified cell lines maintained by ICLAC, provide a scientific rationale for their use.	None are listed.

Animals and human research participants

Policy information about studies involving animals; when reporting animal research, follow the ARRIVE guidelines

11. Description of research animals

Provide all relevant details on animals and/or animal-derived materials used in the study.	No animals were used.

Policy information about studies involving human research participants

12. Description of human research participants

Describe the covariate-relevant population characteristics of the human research participants.	This study did not involve human research participants.